Research Article

Islam Kholidy, Muhammad Hussain Bin Sabt*, Hanafy Mahmoud Abd El-Salam, Mohamed Shaban, and Mohamed Rabia

Enhanced electrochemical synthesis of Ni–Fe/brass foil alloy with subsequent combustion for high-performance photoelectrode and hydrogen production applications

https://doi.org/10.1515/gps-2025-0061
received March 17, 2025; accepted August 27, 2025

Abstract: This study presents a novel approach to synthesizing and characterizing Cu–Fe–Ni ternary alloy and oxide nanostructures for advanced electrochemical and photocatalytic applications. Using electrodeposition on brass substrates from tailored solutions of Nickel(II)chloride, nickel(II) sulfate, and iron(III) chloride, five distinct alloy compositions were fabricated with optimized morphologies and electrochemical properties. Notably, succinic acid was identified as an effective additive, enhancing deposition quality and catalytic activity. A unique ternary alloy oxide was further synthesized via controlled combustion at 950°C. Comprehensive characterization using X-ray diffraction, X-ray photoelectron spectroscopy, scanning electron microscope, Energy dispersive X-ray, and cyclic voltammetry revealed significant structure–property relationships. Alloys formed with higher Ni and Fe chloride concentrations showed rough, agglomerated surfaces, correlating with improved hydrogen evolution reaction performance in alkaline sodium hydroxide. Among all samples, Alloy(v) exhibited the highest hydrogen production efficiency. Furthermore, the alloy oxide demonstrated remarkable photovoltaic potential, delivering current densities of 23 $mA{\cdot}cm^{-2}$ in the dark and 68.45 $mA{\cdot}cm^{-2}$ under illumination. These findings showcase a cost-effective, scalable method for producing multifunctional Cu–Fe–Ni-based materials with dual capabilities in hydrogen generation and solar energy conversion – highlighting a new direction in renewable energy material development.

Keywords: Ni–Fe/brass foil alloy, hydrogen generation, high efficiency, water splitting

1 Introduction

A material's surface is where interactions between its mechanical, thermal, chemical, and electrochemical properties begin. Thus, the surface is the most crucial engineering component of a material. The application of surface modification technologies is indispensable in modern production processes due to evolving standards. The most critical areas of surface technology are tribology and corrosion [1] because surfaces are frequently threatened by wear and corrosion, leading to significant economic and industrial losses if not managed properly. Surface technology can prevent or delay such damage, making it essential in industrial engineering processes. Choosing the best technique to modify surface attributes involves complex decisions often guided by economic and environmental research [2]. One traditional yet effective surface modification technique is electrodeposition [3–5]. With advancements such as Volta's galvanic cell around 1,800, electrodeposition became more efficient for creating coatings through electrochemical processes at the electrode/electrolyte interface. These coatings can enhance a substrate's solderability, lubrication, electrical conductivity, corrosion resistance, wear resistance, and heat resistance.

* **Corresponding author: Muhammad Hussain Bin Sabt**, Chemistry Department, Faculty of Science, University of Kuwait, P.O. Box 5969, Safat, 13060, Kuwait, e-mail: mohammad.binsabt@ku.edu.kw, tel: +965 24985587; fax: +965 24816482
Islam Kholidy: Department of Chemistry, Faculty of Science, Polymer Research Laboratory, Beni-Suef University, BeniSuef, 62514, Egypt; Chemistry Department, Faculty of Science, University of Kuwait, P.O. Box 5969, Safat, 13060, Kuwait
Hanafy Mahmoud Abd El-Salam: Department of Chemistry, Faculty of Science, Polymer Research Laboratory, Beni-Suef University, BeniSuef, 62514, Egypt
Mohamed Shaban: Department of Physics, Faculty of Science, Islamic University of Madinah, P.O. Box 170, Al-Madinah Almonawara, 42351, Saudi Arabia
Mohamed Rabia: Nanomaterials Science and Application Lab, Chemistry Department, Faculty of Science, Beni-Suef University, Beni-Suef, 62511, Egypt

Electrodeposition can be performed using direct current or pulse current (PC), with PC offering benefits like improved element dispersion, nonporous nanostructures, reduced gas absorption, less need for organic additives, and lower environmental impact [6,7]. Nickel (Ni) and its alloys, particularly Ni–Fe, are highly valued in deposition applications due to their excellent corrosion and wear resistance. Ni electrodeposition accounts for up to 12% of global Ni usage [8], primarily for decorative coatings and various industrial purposes such as restoring eroded metals, enhancing magnetic properties, and preparing surfaces for further treatment [9,10]. Ni–Fe alloy coatings, known for their soft magnetic characteristics and good electrical conductivity, are used in electronics, sensors, communication, and optical industries [11]. Compared to other techniques like sputtering and molecular beam epitaxy, electrodeposition offers advantages such as uniform, flaw-free coatings at lower costs and under less stringent conditions. Electroplating baths commonly use sulfate and chloride solutions due to their economic advantages. As an example, for Fe–Ni alloys is the Permalloy where Fe–Ni alloys possess significant commercial value because of their magnetic properties and thermal expansion coefficient. For instance, the Permalloy, Invar, and other Fe–Ni alloys are ideal materials for all kinds of microelectromechanical system devices [12,13]. Adding Nickel(II)chloride ($NiCl_2$) to sulfate baths enhances solution conductivity and Ni anode dissolution, while chloride baths, although producing harder and more stressed coatings, offer higher current efficiencies due to the catalytic effect of chloride ions [14–17]. Boric acid is often added to these baths to improve current density range, coating appearance, and reduce brittleness by acting as a buffer, thus preventing pH rise at the cathode surface [18–22]. Citric acid is also used as a complexing agent in Ni–Fe electroplating baths, forming stable complexes with Fe^{3+}, Ni^{2+}, and Fe^{2+} ions. However, its addition can decrease current efficiency by increasing the cathode surface pH, leading to hydroxide layer formation [23–25]. Despite this, citric acid's complexing effect can shift the reduction potential of Ni–Fe alloys, increase the diffusion-limited current, and enhance nucleation rates. The global shift toward renewable energy technologies, particularly solar cells, necessitates the development of efficient, storable, and transportable energy carriers. Among various alternatives, hydrogen stands out as a clean, high-energy-density fuel with the potential to replace fossil fuels across multiple sectors. As the most abundant element on Earth, hydrogen can be sustainably generated through water electrolysis, provided that the hydrogen evolution reaction (HER) is catalyzed efficiently. Recent advancements have focused on developing highly active and stable electrocatalysts, particularly in alkaline media, to enhance the reaction performance. Alloy-based electrodes have shown promise due to their synergistic catalytic properties, offering improved charge transfer and surface kinetics [26,27]. Despite considerable progress, the overall efficiency and yield of hydrogen production remain below the thresholds required for large-scale industrial deployment. This limitation highlights the urgent need for further innovation in catalyst design, nanostructuring, and interfacial engineering to maximize hydrogen output. Enhancing H_2 generation efficiency not only boosts the viability of water-splitting technologies but also accelerates the implementation of hydrogen as a mainstream energy vector in fuel cells, grid storage systems, and industrial applications [22]. Therefore, optimizing this systems is a critical step toward realizing a hydrogen-powered future in the context of global decarbonization efforts. This enhancement can be attributed to the transformation of transition metal compounds into their active oxide forms [28,29], as shown in manganese-based photocathodes and nanocomposites [30,31]. Herein, in this study, electrochemical deposition of iron, nickel, and their binary alloys onto brass substrates was achieved using electrolytic baths containing 0.1M $NiCl_2$, 0.1M $NiSO_4$, and varying concentrations of $FeCl_3$. Succinic acid was identified as the most effective additive for stabilizing the deposition process and improving coating quality. Structural, morphological, and electrochemical characterizations were performed using various techniques. EDX analysis confirmed alloy compositions including (8Ni–45Cu–0.3Fe–34.7Zn–12O), (15Ni–36Cu–4Fe–30Zn–15O), (60Ni–14Cu–3Fe–21Zn–2O), (18Ni–63Cu–8Fe–10Zn–1O), and (70Ni–7Cu–18Fe–4Zn–1O). Additionally, a thermally oxidized alloy synthesized at 950°C yielded a mixed oxide composition of (52Ni–8Fe–5Cu–4Zn–31O). X-ray diffraction (XRD) patterns revealed dominant alloy phases alongside minor oxide components, providing insights into crystallographic structure and phase distribution. Surface morphology studies indicated that increased concentrations of Ni^{2+} and Fe^{3+} resulted in more aggregated and rougher surface textures compared to deposits enriched in Cu^{2+}. Under alkaline conditions, the Ni–Fe alloys demonstrated high catalytic activity toward the HER, facilitating water molecule reduction and efficient hydrogen gas evolution. The favorable hydrogen adsorption free energies on Ni–Fe active sites support their potential as cost-effective, high-performance electrocatalysts for sustainable hydrogen production in diverse electrolyte systems.

1.1 Experimental details

$NiCl_2$ (99%), nickel(II) sulfate (Ni_2SO_4 99%), sodium hydroxide (NaOH 99%), sodium sulfate (Na_2SO_4 99%), $FeCl_3$ (99%), boric acid 99%, citric acid 99%, tartaric acid 99%, succinic acid 99% (Sigma Aldrich), and (77Cu-33Zn) Foil (Sigma Aldrich 99.99%).

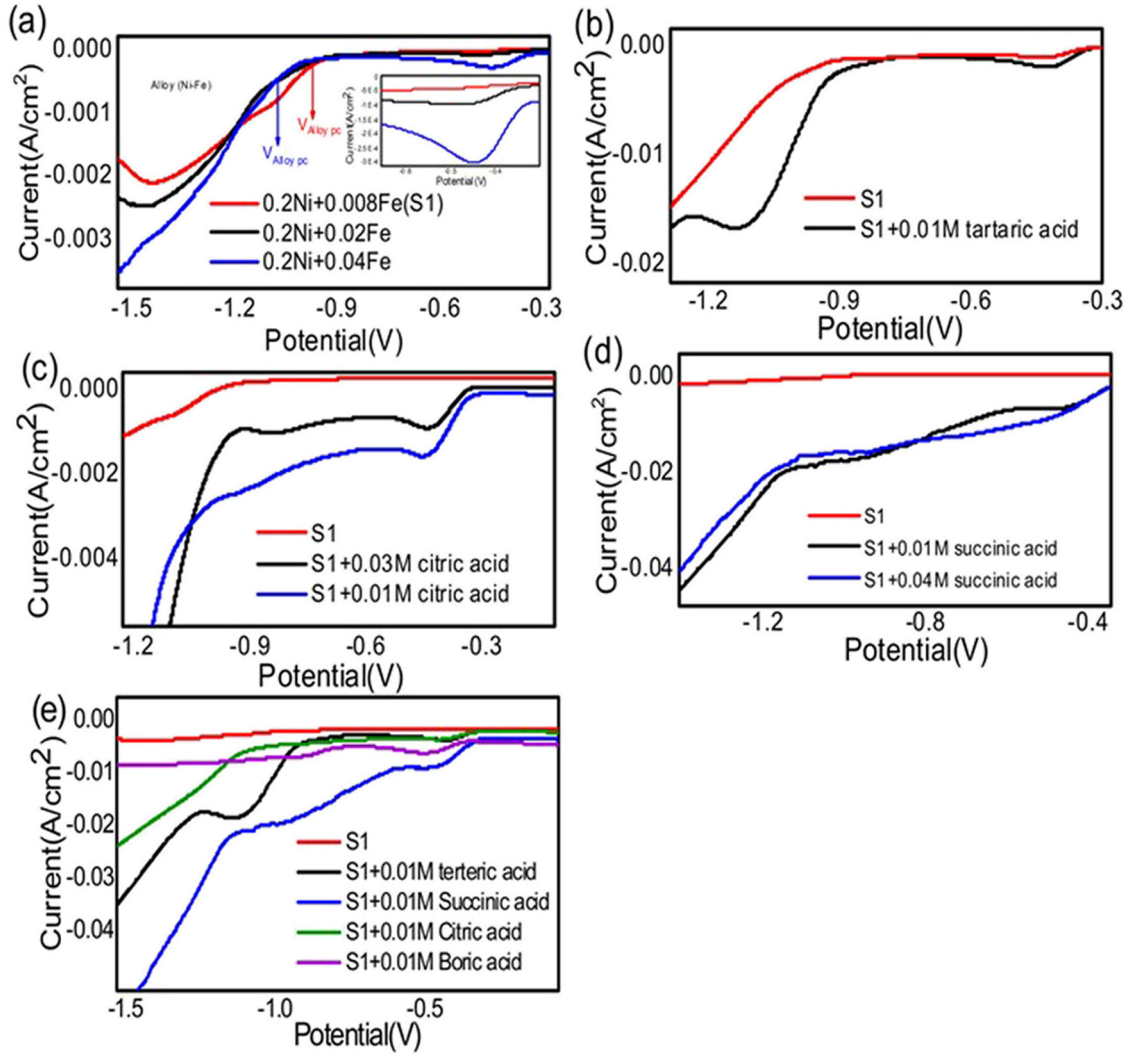

Figure 1: Electrochemical cyclic voltammetry of $NiCl_2$, $NiSO_4$, and $FeCl_3$ dissolved in distilled water electrolyte where (a) 0.1M $NiCl_2$, 0.1M $NiSO_4$, and (0.008–0.04) M $FeCl_3$; (b) 0.1M $NiCl_2$, 0.1M $NiSO_4$, 0.008M $FeCl_2$(S1), and S1 with 0.01M of tartaric acid; (c) S1 with (0.01 to 0.03)M of citric acid; (d) S1 and (0.01–0.04)M of succinic acid; and (e) S1 and S1 with 0.01M of citric acid, 0.01M succinic acid, 0.01M boric acid, and 0.01M tartaric acid at 50 mV s^{-1} and room temperature.

1.2 Samples characterization

The scanning electron microscope (SEM) analysis was performed using a Quanta 250 FEG microscope (FEI Company, Eindhoven, Holland), and the chemical compositions were carefully examined using the accompanying energy-dispersive X-ray unit (EDX). For quantitative analysis, the XRD charts of the deposited alloys were assessed using a Phillips model PW 1730 X-ray generator, a PW 1716 diffractometer, and a PW 1050/25 detector. A copper (Cu) anode with a wavelength of 0.154 nm was utilized, with an ascending voltage of 40 kV, a current of 35 mA, and a scanning rate of 0.02 within a 2θ angle range of 10° to 80°. To study the binding energy and ion valence state of the specimens, X-ray photoelectron spectroscopy (XPS) was carried out using a Thermo ESCALAB 250 Xi instrument. Survey spectra were recorded over a range of 0–1,100 eV for each composition. Additionally, high-resolution spectra were obtained for the $2p_{1/2}$ and $2p_{3/2}$ levels of Fe, Ni, and Zn, as well as for the 1s level of oxygen.

1.3 Electrodeposition of Ni–Fe alloy

Cyclic voltammetry results indicate that, in comparison to other additives, succinic acid emerges as the most effective additive. Figure 2a–d displays cyclic voltammograms for a solution containing both Ni and Fe ions that were measured using an electrochemical cyclic voltammetry technique. The scan rate used was 50 mV·s^{-1}, and the potential range was −2.0 to +2.0 V. The purpose of the experiment was to

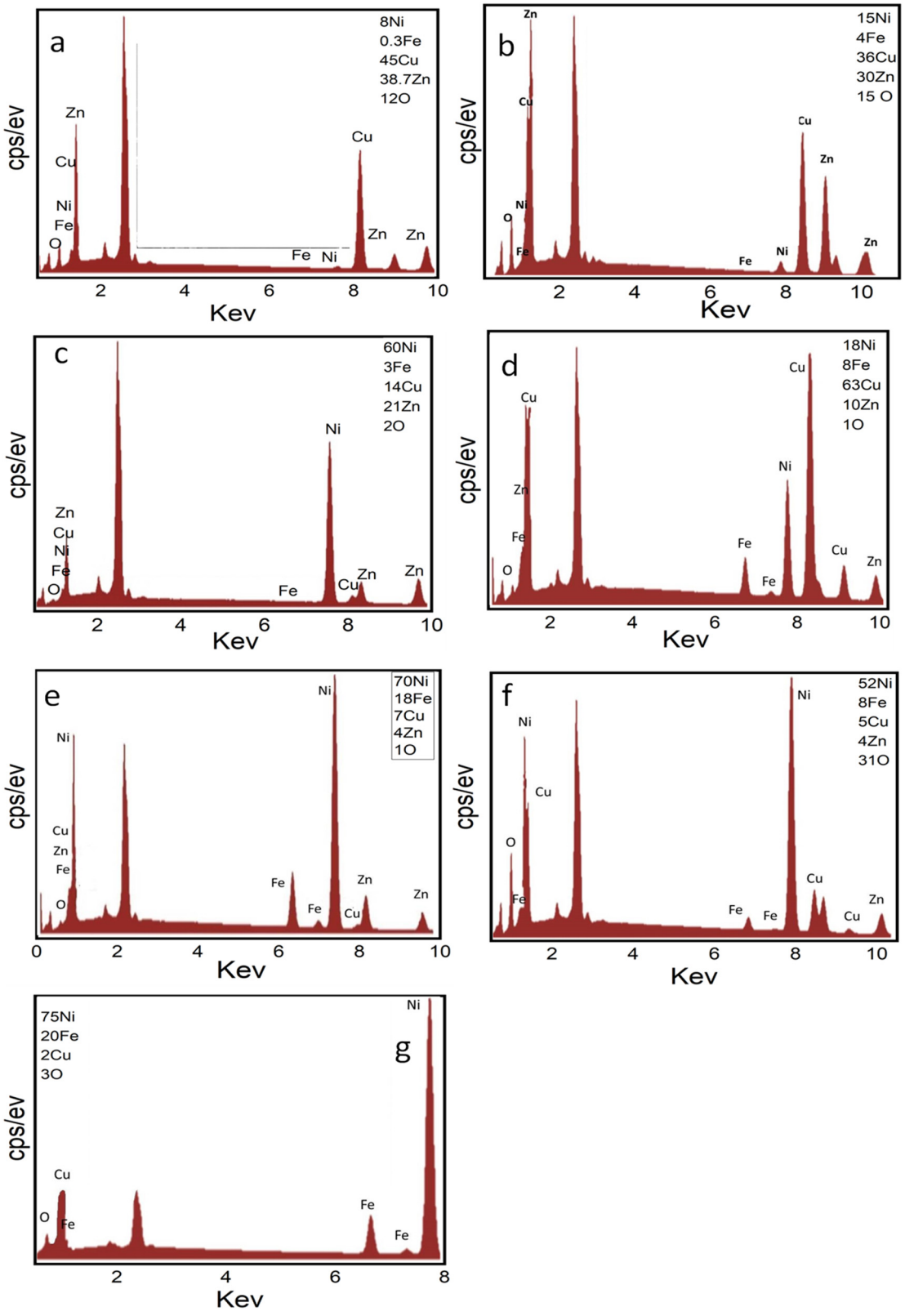

Figure 2: EDX spectra of Ni–Fe–Cu–Zn–O alloys: (a) Alloy I, (b) Alloy II, (c) Alloy III, (d) Alloy IV, (e) Alloy V, (f) the corresponding alloy oxide, and (g) cross-sectional analysis of Alloy IV.

determine the appropriate current and potential for the electrodeposition process. A double jacket cell was used, which contained Pt electrodes as working and counter electrodes and a saturated calomel electrode as a reference electrode. The solution used in the experiment contained $NiCl_2$, $NiSO_4$, and $FeCl_3$ dissolved in a distilled water electrolyte. The results presented in Figure 2a–d show the cyclic voltammograms obtained for this solution under the given experimental conditions. The information obtained from these measurements can be used to determine the optimal conditions for electrodeposition of Ni and Fe ions from this solution. Table 1 shows the effects of different experimental conditions on the electrochemical behavior of Ni–Fe alloys with additives (a) 0.1M $NiCl_2$, 0.1M $NiSO_4$, and (0.008–0.04) M $FeCl_3$; (b) 0.1M $NiCl_2$, 0.1M $NiSO_4$, 0.008M $FeCl_2$(S1), (S1) with 0.01M of tartaric acid; (c) (S1) with (0.01–0.03)M of citric acid; (d) (S1) with (0.01–0.04) M of succinic acid; and (e) S1 with 0.01M of citric acid, S1 with 0.01M succinic acid, S1 with 0.01M boric acid, and S1 with 0.01M tartaric acid) at 50 $mV{\cdot}s^{-1}$ and room temperature.

1.3.1 Determine the best concentration of Ni and Fe

It seems that Figure 1a shows the effects of different experimental conditions on the electrochemical behavior of Ni, Fe, and Ni–Fe alloys. In this figure, it was observed that increasing the concentration of Fe led to an increase in the reduction potential peak of Fe and Ni E_{pcIron} = (−0.34 to −0.42) V, $E_{pc\ Nickel}$ = (−1.2 to −1.7) V, respectively, but a decrease in the reduction potential peak of Ni–Fe alloy $E_{pc\ Alloy}$ = (−1.15 to −0.96) V. The optimal condition for electrodeposition of Ni–Fe alloy was found to be a sample containing (0.008M Fe and 0.2M Ni) (S_1). This sample showed a shift in the reduction potential peak of about 103 mV and an increase in the intensity of the reduction current peak of about 0.2 mA compared to the sample containing 0.2M Ni and 0.04M Fe alloy, where $I_{pc\ Alloy}$ = (−0.6 to −0.8) mA.

1.3.2 Effect of tartaric acid

In Figure 1b, the effect of tartaric acid on the electrochemical behavior of Ni, Fe, and Ni–Fe alloys was studied. It was observed that the presence of tartaric acid led to an increase in the intensity of the current reduction peak of Fe $I_{pc\ Iron}$ = (−1.2 to −2.2) mA, and a shift in the electrodeposition process for Ni–Fe alloy to more positive potentials $E_{pc\ Iron}$ = (–0.5 to –0.34) V. The electrodeposition process for Ni–Fe alloy starts at around $E_{pc\ Alloy}$ = –0.86 V, at more positive potentials than in the absence of tartaric acid $E_{pc\ Alloy}$ = −0.99 V. Figure 1b shows a broad reduction peak for alloy where current reduction peak of alloy increases $I_{pc\ Alloy}$ = (−7 to −16.5) mA. From Figure 1b, we observed that the sample with tartaric acid has the ability to produce higher hydrogen evaluation than the sample without tartaric acid.

1.3.3 Effect of citric acid

According to Figure 1c, the addition of citric acid to the electrolyte solution led to an increase in the intensity of the current reduction peak of Fe $I_{pc\ Iron}$ = (−1 to −1.8) mA at an iron reduction potential peak of $E_{pc\ Iron}$ = −0.45 V. The best concentration of citric acid was found to be 0.01 M, as this concentration resulted in an increase in the intensity of the current reduction peaks of both Fe and Ni–Fe alloy.

Table 1: Effects of different experimental conditions on the electrochemical behavior of Ni–Fe alloys with additive

Figure 1	Samples	Start $E_{pc\ Alloy}$ (V)	Max $I_{pc\ Alloy}$ (mA)	Optimum sample
Figure 1a	0.1M $NiCl_2$ + 0.1M $NiSO_4$ + 0.008M $FeCl_3$(S1)	−1.05	−0.8	S1
	0.1M $NiCl_2$ + 0.1M $NiSO_4$ + 0.02M $FeCl_3$	−0.96	−0.6	
	0.1M $NiCl_2$ + 0.1M $NiSO_4$ + 0.04M $FeCl_3$	−1.1	−0.48	
Figure 1b	S1	−1.05	−0.8	S1 + 0.01M tartaric acid
	S1 + 0.01M tartaric acid	−0.86	−16.8	
Figure 1c	S1	−1.05	−0.8	S1 + 0.01M citric acid
	S1 + 0.01M citric acid	−0.99	16.4	
	S1 + 0.03M citric acid	−0.99	18.2	
Figure 1d	S1	−1.05	−0.8	S1 + 0.01M succinic acid
	S1 + 0.01M succinic acid	−0.77	−18	
	S1 + 0.04M succinic acid	−0.83	−16.3	
Figure 1e	S1	−1.05	−0.8	S1 + 0.01M succinic acid
	S1 + 0.01M tartaric acid	−0.86	−16.8	
	S1 + 0.01M citric acid	−0.99	16.4	
	S1 + 0.01M succinic acid	−0.77	−18	
	S1 + 0.01M boric acid	−0.84	−5	

1.3.4 Effect of succinic acid

Based on Figure 1d, it was observed that an increase in the concentration of succinic acid resulted in an increase in the intensity of the current reduction peak of Fe at an iron reduction potential peak of $E_{\text{pc Iron}}$ = −0.504 V. The optimal concentration of succinic acid was found to be 0.01 M, as it resulted in an increase in the intensity of the current reduction peaks of Ni–Fe alloy, specifically a change in $I_{\text{pc alloy}}$ = (−8 to −16.5) mA and in E_{pc} alloy = (−1.15 to −0.81) V than other concentrations of succinic acid.

1.4 Preparation of photoelectrode

The Ni–Fe/brass composite material that was synthesized is utilized as a photoelectrode for the water splitting reaction (Figure 1(e)). Additionally, the oxides of this alloy, obtained through a combustion process at 950°C for 20 min, are employed as photoelectrodes for hydrogen generation. The hydrogen generation experiments are conducted using a 0.2M Na_2SO_4 electrolyte solution, and a solar simulator emitting light at an intensity of 400 mW·cm^{-2} is employed as the light source. The applied potential ranges from −1.2 to 1 V at room temperature.

2 Results and discussion

2.1 Electrodeposition process and alloy synthesizing

EDX spectra are shown in Figure 2a–g for Ni–Fe–Zn–Cu–O alloys synthesized in distilled water containing (a) Alloy(I), (b) Alloy(II), (c) Alloy(III), (d) Alloy(IV), (e) Alloy(v), (f) Alloy-oxide after deposited and combustion at 950°C for 20 min and (g) is a cross section of alloy(v). The chemical compositions of the examined samples are shown in Table 2. All the spectra show only Fe, Ni, Cu, and Zn and signals without any impurity traces from the used chemicals, which indicate the high purity of the deposited Ni/Fe alloys spectra of Ni–Fe–Zn–Cu–O alloys. The alloys were synthesized in distilled water and various samples were analyzed. The results are presented in Figure 2, with panels (a) to (g) corresponding to different samples. In Figure 2a, the EDX spectrum represents Alloy(I), which was synthesized in distilled water. Similarly, Figure 2b corresponds to Alloy(II), Figure 2c corresponds to Alloy(III), Figure 2d corresponds to Alloy(IV), Figure 2e corresponds to Alloy(v), Figure 2f represents the EDX spectrum of the Alloy-oxide after deposition and combustion at 950°C for 20 min, and Figure 2g shows a cross-section of Alloy(v). The chemical compositions of the examined samples are provided in Table 2. The elements detected in all the spectra are Fe, Ni, Cu, and Zn. No impurity traces from the used chemicals were observed, indicating the high purity of the deposited Ni/Fe alloys. The surface morphology of deposited alloys was studying by a SEM. The study involves two different Ni/Fe alloys formed on the surface of a Cu–Zn foil from distilled water. Additionally, there is mention of an alloy oxide formed after heat treatment at 950°C for 20 min. Figure 3a shows the SEM image of Alloy(I) on the Cu–Zn foil surface, Figure 3b shows the SEM image of Alloy(II) on the Cu–Zn foil surface, Figure 3c shows the SEM image of Alloy(III), shows the Figure 3d SEM image of Alloy(IV), Figure 3e shows the SEM image of Alloy(v), Figure 3f shows the SEM image of Alloy oxide formed after heat treatment at 950°C for 20 min, and Figure 3g shows the cross-section image of Alloy(v). It is stated that the morphology of the alloy can be reformed by governing its chemical composition. In Figure 3a, the Alloy(I) is characterized by spherical grain particles with low density. This is attributed to a low deposition ratio of Nickel and Iron in the alloy formation process. Moving to Figure 3b, Alloy(II) shows a slight increase in the deposition ratio of Nickel and Iron compared to Alloy(I). The addition of

Table 2: Chemical compositions of nano crystalline Ni–Cu–Fe–Zn alloys obtained from EDX analysis where (S1) is 0.1M ($NiCl_2$ + $NiSO_4$) + 0.008M $FeCl_3$

Sample	Bath composition	Additives	Ni%	Cu%	Fe%	Zn%	O%	Applied potential (V)	Case of alloy
A	(S1)	Non	8	45	0.3	34.7	12	−1.05	Alloy(I)
B	(S1)	0.01M boric acid	15	36	4	30	15	−0.85	Alloy(II)
C	(S1)	0.01M citric acid	60	14	3	21	2	−1	Alloy(III)
D	(S1)	0.01M tartaric acid	18	63	8	10	1	−0.86	Alloy(IV)
E	(S1)	0.01M succinic acid	70	7	18	4	1	−0.77	Alloy(v)
F	(S1)	0.01M succinic acid	52	5	8	4	31	−0.77	Alloy-oxide
G	(S1)	0.01M succinic acid	70	7	18	4	1	−0.77	Section of alloy(v)

boric acid leads to an increased number of deposited particles in Nickel and Iron, resulting in a slightly higher deposition ratio. Figure 3c demonstrates the significant effect of citric acid in the deposition process, particularly in Nickel deposition. There is a noticeable improvement in the deposition of Nickel, as well as a slight enhancement in the deposition of Iron. However, some agglomeration is observed between the particles of Iron and Nickel, indicating a possible

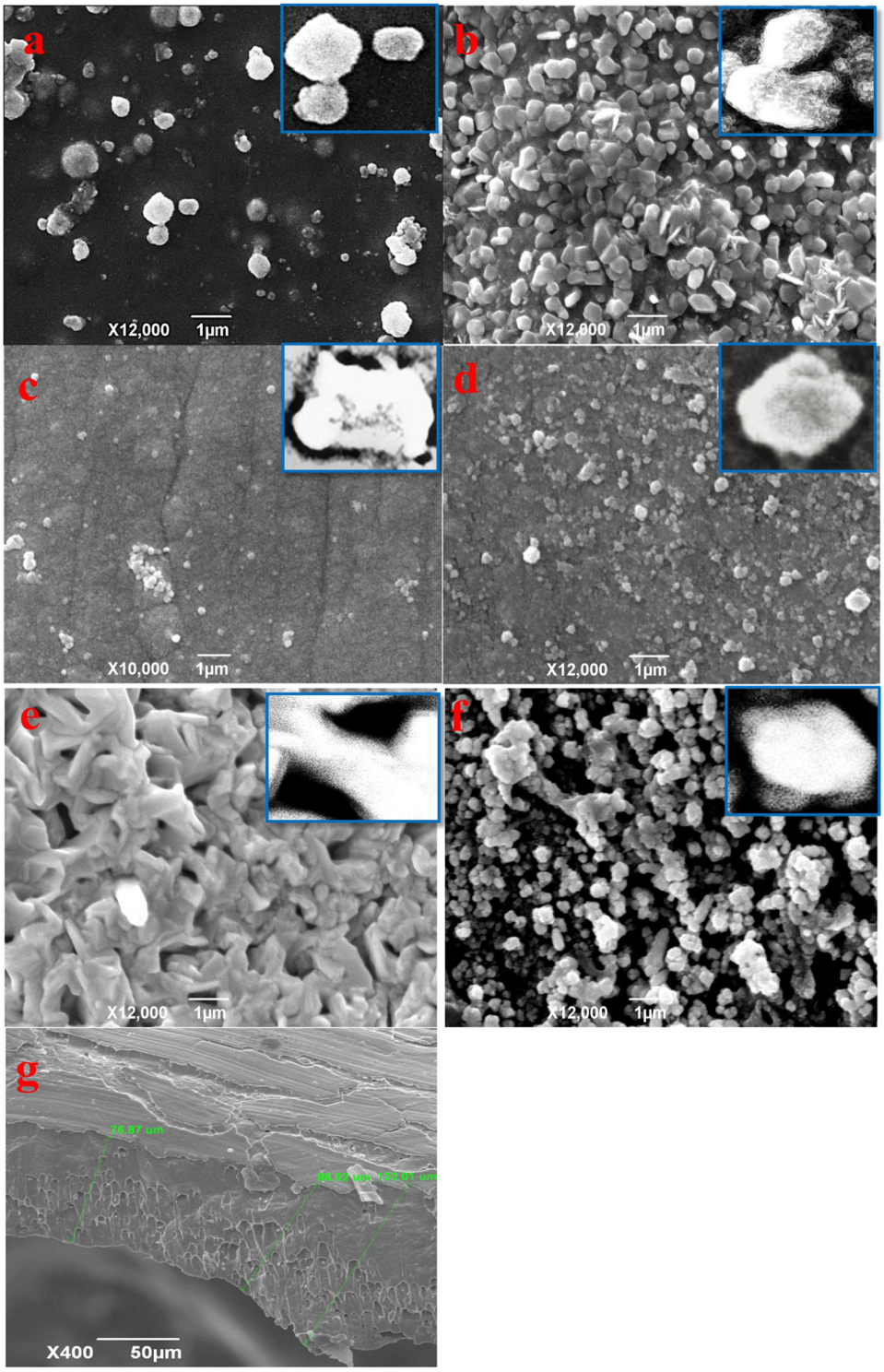

Figure 3: SEM images of Cu–Fe–Ni–Zn–O alloys: (a) Alloy I, (b) Alloy II, (c) Alloy III, (d) Alloy IV, (e) Alloy V, (f) the corresponding alloy oxide, and (g) cross-sectional view of Alloy V.

interaction or collection between them. Figure 3d showcases the influence of tartaric acid, which has a very good effect on Iron deposition and a good effect on Nickel deposition. The result is a well-distributed composition between Iron and Nickel in the thin film. The presence of small overlapping grains indicates a good quality of deposit, suggesting a desirable structure for the alloy. Moving on to Figure 3e, Alloy(v) stands out as the best sample among the presented images. It contains the highest ratio of Nickel and Iron. Additionally, it exhibits a high number of bonds, resembling a thread mesh structure. This indicates a strong interconnectivity within the alloy and suggests a structurally robust composition. The percent composition of the Ni–Fe alloy in the thin film becomes dominant, contributing to the enhanced strength and structural integrity. Figure 3f focuses on the alloy oxide formed after heat treatment. Following the determination that Alloy (v) is the best sample, heat treatment is performed at 950°C. The SEM image shows clear small granular crystals of Ni–Fe metal uniformly deposited on the surface of the Cu–Zn substrate. This result suggests good adhesion between the Ni–Fe deposit and the Cu–Zn substrate, indicating a strong interface between the two materials. Finally, Figure 3g displays the cross-section of Alloy(v), offering insight into the thickness layer of the alloy. The image indicates a very good thickness distribution, highlighting the effectiveness of the deposition process in achieving a uniform and controlled thickness for the alloy. Taken together, the SEM images provide valuable information about the influence of deposition conditions and chemical compositions on the morphology and characteristics of the Ni/Fe alloys. The variations observed in grain size, density, distribution, and structural integrity underscores the importance of carefully controlling the deposition parameters to tailor the alloy properties according to desired specifications. Alloy(v) exhibited a well-defined network and fibrous morphology, with individual fiber diameters ranging from approximately 200 to 250 nm. This unique structure significantly enhances the surface area, which is highly beneficial for the HER. In contrast, Alloys(I) through (IV) primarily displayed radial particle morphologies, with particle diameters decreasing from around 500 nm in Alloy(I) to approximately 200 nm in Alloy(IV). Although Alloy(IV) shares a comparable particle size with Alloy(v), the latter demonstrates superior catalytic potential due to its interconnected fiber network and improved structural uniformity. These morphological features of Alloy(v) are believed to facilitate better charge transfer and active site exposure, thereby enhancing the efficiency of H_2 gas generation.

2.2 Structural properties of the prepared nanomaterials

The structural properties of the prepared nanomaterials, before (alloys) and after the combustion process, were investigated using XRD. Figure 4 shows XRD charts for

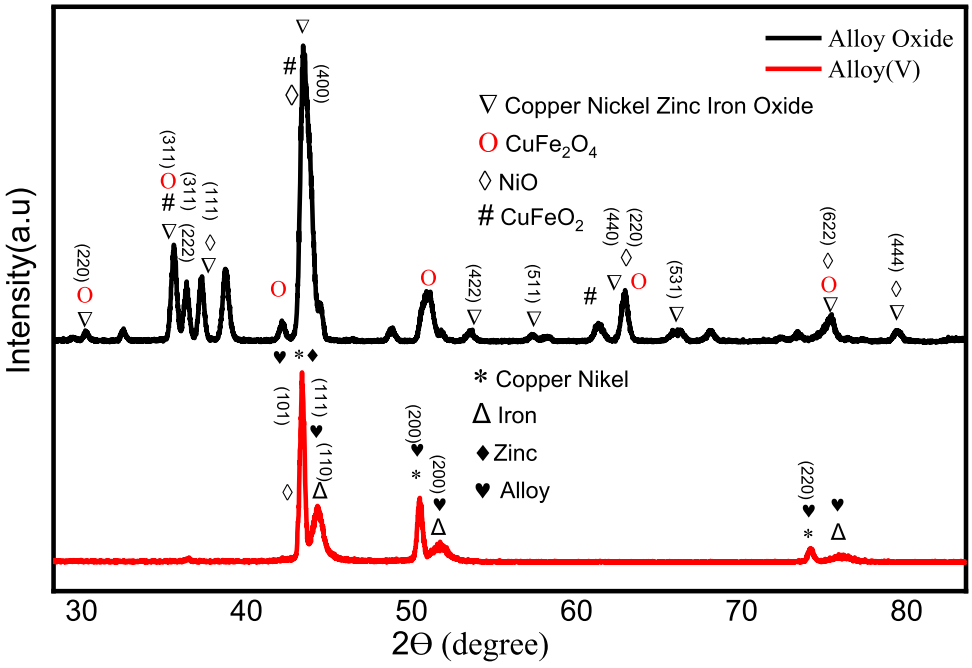

Figure 4: XRD charts for the alloy prepared from where Alloy(v) is, Alloy oxide is Alloy(v) after combustion at 950°C for 20 min.

Alloy(v) alloys deposited from different solutions of nickel and iron. Figure 4 displays the XRD pattern for the alloy prepared from the electrolyte: 0.1M $NiCl_2$, 0.1M $NiSO_4$, 0.008M $FeCl_3$ (S1) with 0.01M succinic acid (Alloy v), and after combustion at 950°C (Alloy oxide). Figure 4 clearly demonstrates the polycrystalline nature of all deposited Ni/Fe-based films. For the Alloy(v), peaks related to the Ni/Fe alloy were observed at 2θ = 43.42° (111), 50.52° (200), and 74.21° (220) planes, corresponding to CuNi crystals (JCPDS card No. 00-009-0205); a peak at 2θ = 43.28° (101) for Zn crystals (JCPDS card No. 00-004-0784); peaks at 2θ = 44.47° (110), 52.73° (200), and 76.01° (211), corresponding to Fe crystals (JCPDS card No. 01-081-8767); a peak at 2θ = 43.25° (200) for NiO crystals (JCPDS card No. 04-0835) [32], peaks at 2θ = 35.65° (012), 43.24° (104), and 60.99° (110) corresponding to $CuFeO_2$ nanoparticles (JCPDS card No. 75-2146). These peaks confirm the presence of Ni/Fe alloy phases. For the alloy oxide after combustion, peaks were observed at 2θ = 30.24° (220), 35.58° (311), 36.35° (222), 43.71° (400), 53.54° (422), 57.12° (511), 62.91° (440), 66.20° (531), 75.28° (533), and 79.34° (444), corresponding to $(Fe_{0.8}{\cdot}Zn_{0.2})(Ni_{0.6}{\cdot}Cu_{0.2}{\cdot}Fe_{1.2})O_4$ spinel oxide structure (JCPDS card No. 01-081-8585); peaks at 2θ = 37.23° (111), 43.25° (200), 62.82° (220), 75.28° (311), and 79.43° (222) for NiO crystals (JCPDS card No. 04-0835); and peaks at 2θ = 30.32° (220), 35.52° (311), 37.19° (222), 43.25° (400), 51.30° (511), 62.94° (440), and 75.38° (533) for $CuFe_2O4$ (JCPDS card No. 00-025-0283). These results indicate that the final oxide material is a multimetal oxide system comprising Cu, Ni, Zn, and Fe integrated into a spinel-like structure.

2.3 XPS

The XPS spectrum presented in Figure 5a–h clearly indicates the presence of several elements, including Ni, Cu, Fe, Zn, and O in the alloy. This observation is consistent with the elemental mapping results discussed earlier. In particular, Figure 5a and g represents Alloy(v), while Figure 5h and n represents Alloy Oxide. Figure 5g and n shows distinct peaks centered at 1022.32 and 1045.40 eV, which can be attributed to Zn_{2P} species. Additionally, Figure 5c and j displays peaks corresponding to Cu_{LM2}, and Figure 5f provides detailed XPS spectra of Cu_{2p}. Figure 5d provides detailed XPS spectra of Fe_{2p} spectra, exhibit peaks at 712.5 eV, which can be assigned to Fe ions. Furthermore, the spectrum in Figure 5b reveals high-resolution XPS spectra of O_{1s}, with peaks observed at 529.3, 531.27, and 532.22 eV. After fitting with Gaussian–Lorentzan functions, three peaks are identified. The peak at 529.3 eV corresponds to the lattice oxygen peak in the O_{1s} spectrum of polycrystalline NiO [33,34]. The provided information suggests that in the Ni_{2p} region, there is evidence of bulk metal content supporting the compositional analysis previously discussed. In Figure 5e, the spectra of nickel display a distinct and sharp peak, indicating the presence of metallic nickel. The multiple structures observed in the Ni_{2p} spectra are identical to the spectra reported for NiO. Moving on to Figure 5i, the O_{1s} spectrum of metal oxides displays two peaks. A low binding energy feature is observed at 530.1 eV, which is attributed to the lattice oxygen in metals oxide. Additionally, a high binding energy (HBE) feature is observed at 531.5 eV. In the O_{1s} spectrum of different metal oxides including Cu–Fe–Ni–Zn oxide, the lattice oxygen peak was found at 529.3 eV with an HBE feature at 531.1 eV, as reported by researchers [33–37]. The HBE feature in the O_{1s} spectrum is discussed in the literature to arise from oxygen defects or adsorbed oxygen. Furthermore, in summary, the features observed in the XPS spectra provide evidence that the sample contains Ni, Fe, Cu, and Zn. The high-resolution XPS spectra of O_{1s} were observed and fitted using Gaussian–Lorentzian functions. In Figure 5k, the high-resolution XPS spectra of Fe_{2p} and O_{1s} are displayed. The peaks observed at 724.18 and 709.42 eV can be associated with the characteristic signals of $Fe_{2p1/2}$ and $Fe_{2p3/2}$, respectively. Additionally, two broad peaks at 732.16 and 718.4 eV are attributed to satellite peaks of Fe. The $Fe_{2p3/2}$ peak can be further divided into three distinct peaks at binding energies of 712.9, 710.65, and 709.43 eV, respectively, the presence of these three peaks indicates the presence of Fe–O bonds. These results provide confirmation of the formation of iron oxide within the sample. In Figure 5l, the XPS spectra of nickel exhibit well-defined and sharp peaks, signifying the presence of nickel in multiple oxidation states. The presence of a satellite peak confirms the existence of NiO or another Ni^{2+} species. Additionally, the observed chemical shifts in the $2p_{1/2A}$ and $2p_{3/2A}$ peaks indicate that nickel is present in distinct chemical environments. Figure 5m reveals important information about the oxidation states of copper in the $CuFe_2O_4$ sample. Strong Cu^{2+} satellites can be observed at binding energies of 942.5 and 962.5 eV, in addition to a peak at 934.3 eV. This indicates the presence of Cu^{2+} in $CuFe_2O_4$, as reported in the literature [38,39]. Furthermore, based on the relatively lower peak at 932.1 eV, it can be inferred that there are Cu^{+} species on the surface of $CuFe_2O_4$ [40]. The XPS spectra provide strong evidence for the presence of $CuFeO_2$ in the sample. The $Fe2p_{3/2}$ peak at 709.43 eV, observed in Figure 5k, indicates the presence of Fe–O bonds, consistent with iron oxide compounds. Additionally, the $Cu2p_{3/2}$ peak at 934.3 eV, along with satellite peaks

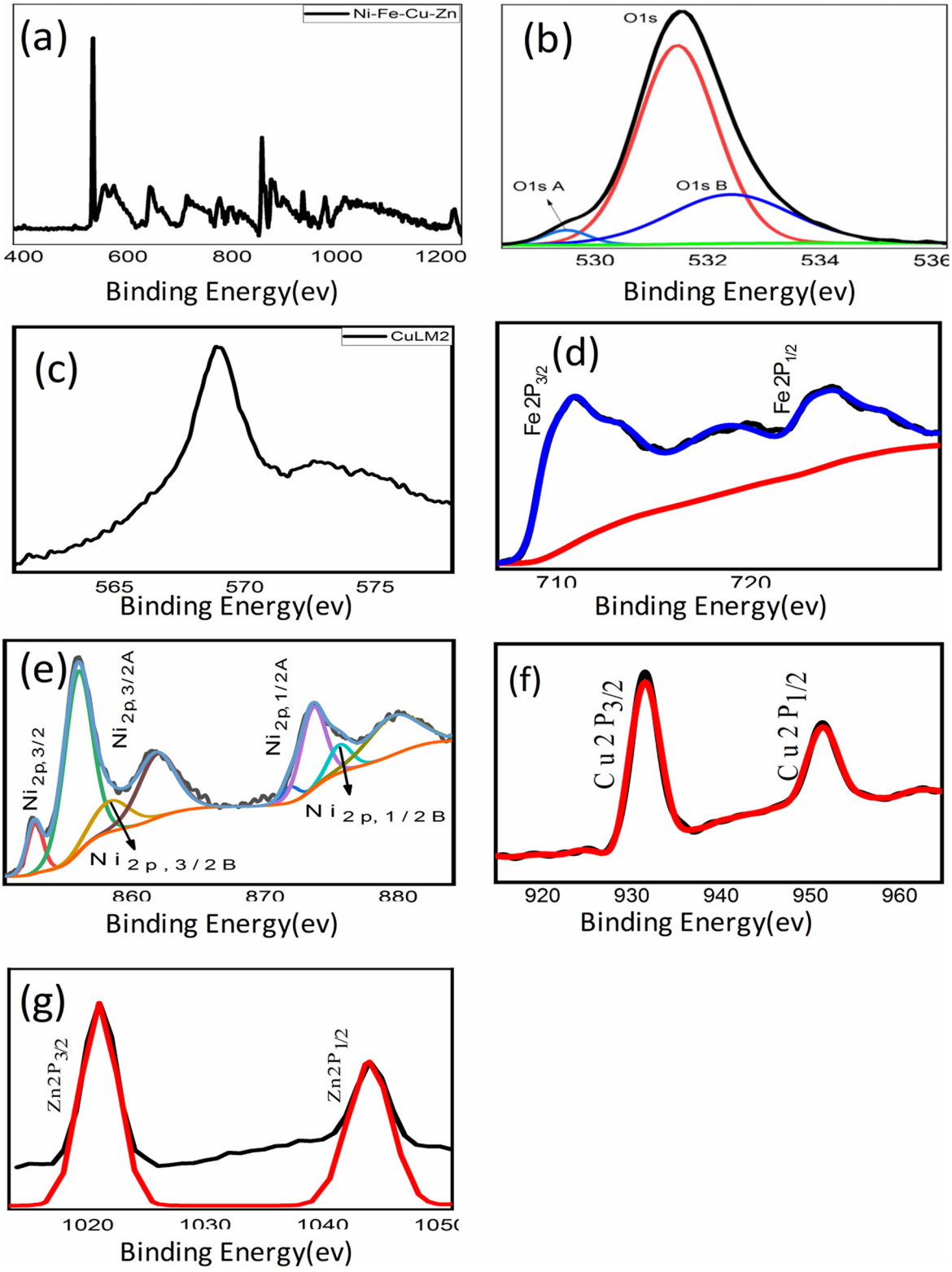

Figure 5: XPS spectrum of the as-prepared Alloy(v): (a) survey spectrum of Ni–Cu–Fe–Zn–O, (b) binding energy spectrum of $O_{(1S,ISA,B)}$, (c) binding energy spectrum of Cu_{LM2}, (d) binding energy spectrum of Fe_{2P}, (e) binding energy spectrum of $Ni_{2P(3/2,1/2)}$, (f) binding energy spectrum of $Cu_{2P(3/2,1/2)}$, (g) binding energy spectrum of Zn_{2P}, (h) survey spectrum of alloy oxide for Ni–Cu–Fe–Zn–O, (i) binding energy spectrum of $O_{(1S,ISA)}$, (j) binding energy spectrum of Cu_{LM2}, (k) binding energy spectrum of $Fe_{2P(3/2,1/2)}$, (l) binding energy spectrum of $Ni_{2P(3/2,1/2)}$, (m) binding energy spectrum of $Cu_{2P(3/2,1/2)}$, and (n) binding energy spectrum of Zn_{2P}.

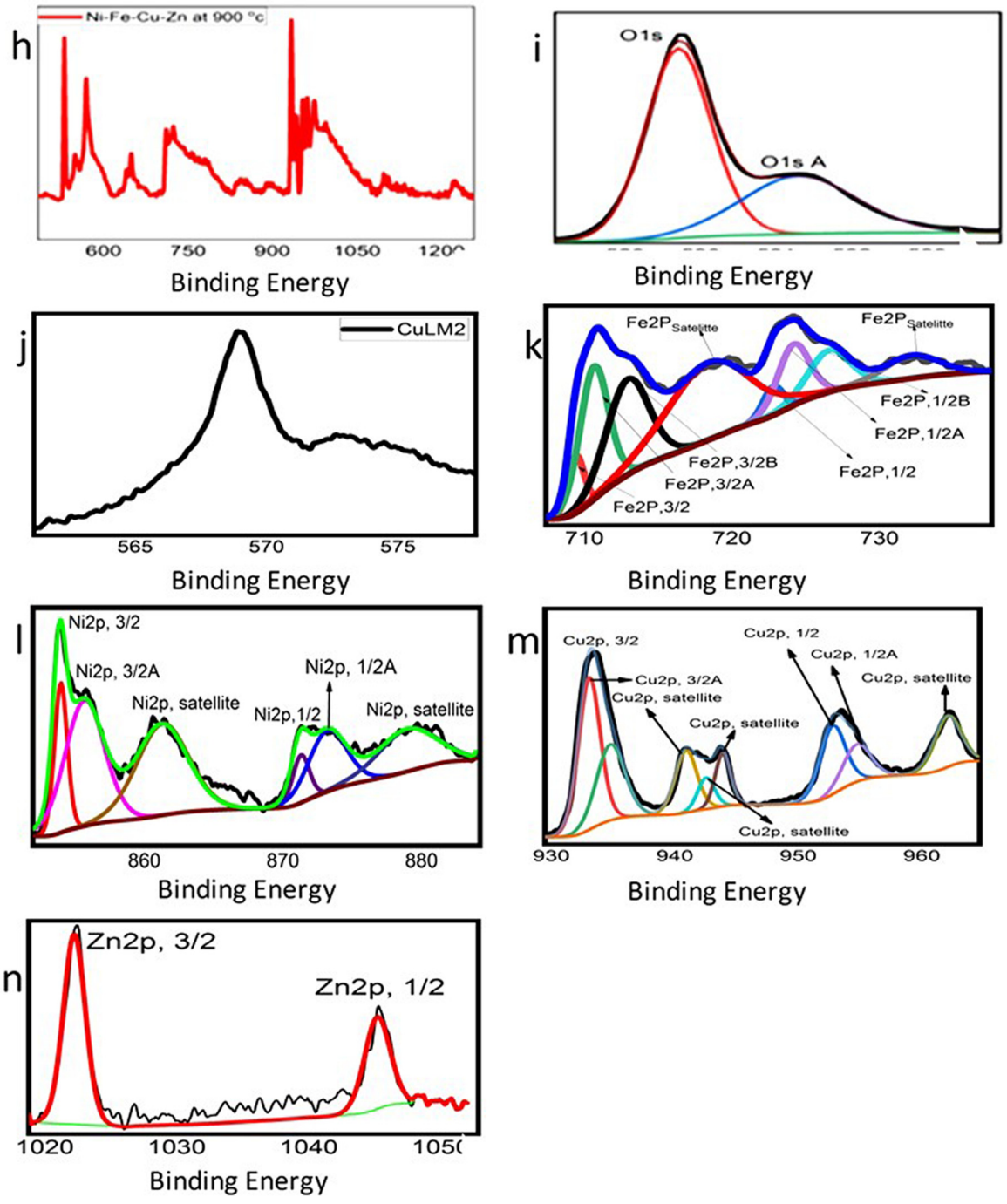

Figure 5: (*Continued*)

at 942.5 and 962.5 eV in Figure 5m, confirms the presence of Cu^{2+} species. The lower peak at 932.1 eV further suggests the existence of Cu^{+} species, which are characteristic of $CuFeO_2$. The O_{1s} spectrum in Figure 5i shows peaks at 530.1 and 531.5 eV [35,37], corresponding to lattice oxygen in metal oxides and oxygen defects, respectively, aligning with the reported values for $CuFeO_2$. Literature [38–40] support these binding energies, specifically for the coexistence of Cu^{+} and Cu^{2+} in the structure of $CuFeO_2$. Together, these findings indicate the formation of $CuFeO_2$ within the sample, corroborating the XPS results with the known chemical structure of $CuFeO_2$. The XPS spectra showed the presence of $CuFeO_2$ in the sample. The $Fe2p_{3/2}$ peak at 709.43 eV, observed in Figure 5k, indicates the presence of Fe–O bonds, consistent with iron oxide compounds. Additionally, the $Cu2p_{3/2}$ peak at 934.3 eV, along

with satellite peaks at 942.5 and 962.5 eV in Figure 5m, confirms the presence of Cu^{2+} species. The lower peak at 932.1 eV further suggests the existence of Cu^{+} species, which are characteristic of $CuFeO_2$. The O_{1s} spectrum in Figure 5i shows peaks at 530.1 and 531.5 eV, corresponding to lattice oxygen in metal oxides and oxygen defects, respectively, aligning with the reported values for $CuFeO_2$. Literature [38–40] support these binding energies, specifically for the coexistence of Cu^{+} and Cu^{2+} in the structure of $CuFeO_2$. Together, these findings indicate the formation of $CuFeO_2$ within the sample. The XPS analysis confirms the formation of the Copper Nickel Zinc Iron Oxide compound through the detection of Fe, Zn, Ni, Cu, and O in their characteristic oxidation states. The Fe 2p spectrum exhibits peaks at 724.18 and 709.42 eV [37], with satellite peaks at 732.16 and 718.4 eV, confirming Fe^{2+}/Fe^{3+} oxidation states. Zn^{2+} is identified by peaks at 1022.32 and 1045.40 eV, indicating its substitution in the spinel lattice. Ni^{2+} is confirmed by a peak at 855.6 eV, while Cu^{2+} is identified at 934.3 eV, with satellites at 942.5 and 962.5 eV, suggesting Cu–Fe interactions. The O_{1s} spectrum exhibits a peak at 529.3 eV [33,34], characteristic of metal-oxygen bonding in spinel structures. The observed binding energy shifts confirm strong cationic interactions, indicative of a mixed-metal oxide rather than separate oxides. The fitting of Fe, Ni, Cu, and Zn peaks with Gaussian–Lorentzian functions further supports their incorporation in a single-phase ferrite structure.

2.4 Open-circuit potentials measurements

In an alkaline medium such as 0.5 mol·L^{-1} NaOH, the OCP reflects the equilibrium between anodic (e.g., metal oxidation or dissolution) and cathodic (e.g., water or proton reduction) surface processes [41,42]. A more negative OCP signifies a surface that is more reducing, indicating that the cathodic reaction specifically HER is thermodynamically more favorable (Figure 6). Therefore, a material exhibiting a lower (more negative) OCP is closer to the HER potential and typically requires less overpotential to initiate hydrogen evolution. In our study, Alloy(v) displayed the most negative steady-state OCP among the five alloys tested. This implies a higher driving force for electron transfer to water molecules, thereby enhancing the tendency for HER to occur on its surface. Additionally, the more negative potential may also indicate a less stable or thinner passive film, which facilitates electron availability for HER instead of passivation [41,42]. In summary, the significantly negative OCP observed for Alloy(v), combined with its known composition and surface characteristics, strongly suggests that it is electrochemically predisposed to promote hydrogen generation, validating our conclusion from the OCP measurements.

2.5 Electrocatalytic activities

The Cu–Fe–Ni–Zn–O alloy system demonstrates significant potential for efficient hydrogen gas generation from alkaline media, particularly NaOH solutions. This multimetallic oxide alloy exhibits a synergistic catalytic behavior that enhances the HER by offering a high density of active sites and promoting rapid electron transfer. The presence of nickel and copper oxides contributes to improved electrical conductivity and catalytic activity, facilitating the adsorption and reduction of water molecules. Meanwhile, iron and zinc oxides modulate the electronic structure of the surface, optimizing hydrogen adsorption energy and enhancing overall reaction kinetics. In an alkaline NaOH environment, the HER mechanism typically follows:initially, water molecules are reduced to form adsorbed hydrogen intermediates (H^{*}) and hydroxide ions. These intermediates then combine either electrochemically with another electron and water molecule to form hydrogen gas or recombine directly. The redox-active nature of the alloy, particularly through Fe^{3+}/Fe^{2+} and Ni^{3+}/Ni^{2+} transitions, supports continuous electron cycling and catalytic stability. Moreover, the mixed oxide structure enhances corrosion resistance, allowing for long-term

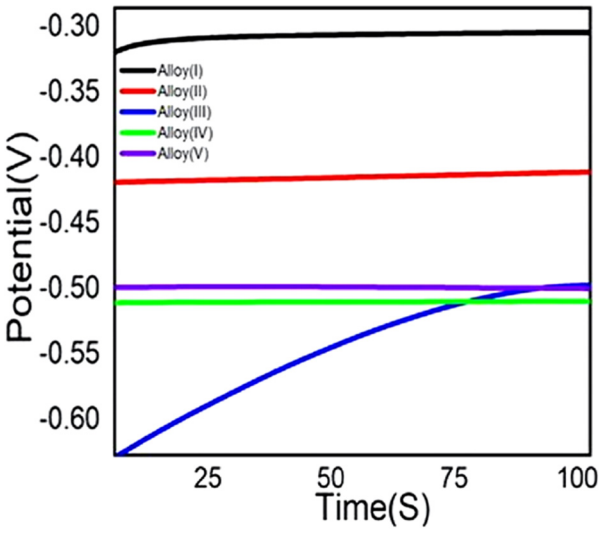

Figure 6: Variation of the open-circuit potential with time for substrate of Alloy(I, II, III, IV, V) immersed in stagnant aerated 0.5 mol·L^{-1} NaOH solution at 25°C.

operation in harsh alkaline environments. Overall, Cu–Fe–Ni–Zn–O alloys offer a robust, cost-effective platform for green hydrogen generation. HERs can occur in alkaline mediasuch as (NaOH), and the electrochemical polarization (ECP) mechanism plays a crucial role in this case. The HER also proceeds through an ECP mechanism. In an alkaline medium, the hydroxide ions (OH^-) are the source of protons for the HER. The overall reaction ($2OH^- + 2e^- \rightarrow H_2O + 2OH^- \rightarrow H_2 + 2O^{2-}$). Here, two hydroxide ions (OH^-) are reduced to produce water (H_2O) and generate hydrogen gas (H_2) as a product. The reaction proceeds through a similar series of steps. Hydroxide ions are adsorbed onto the electrode surface, followed by electron transfer to form adsorbed hydroxyl radicals (OH^*) [42]. These radicals then combine to form water and release hydrogen gas. In an alkaline media, the ECP mechanism governs the HER and involves the adsorption, electron transfer, and desorption of species on the electrode surface. The kinetics and efficiency of the HER in each medium can be influenced by factors such as the electrode material, electrolyte concentration, temperature, and applied potential. Understanding the HER in alkaline medium is crucial for various applications, including hydrogen fuel cells, electrolyzers, and renewable energy storage. By studying the ECP mechanisms in an alkaline medium, researchers can develop efficient electrocatalysts and optimize operating conditions for hydrogen production. In summary, HERs using the electrochemical polarization (ECP) mechanism occur in an alkaline (NaOH) medium. hydroxide ions are reduced in the alkaline medium [42].

The electrocatalytic activity of Cu–Fe–Ni–Zn–O cathodes with varying percentages of Ni and Fe was investigated for HERs in 1M NaOH solution. The experiment involved calibrating the measured potential with respect to the NHE using the Nernst equation. The experimentally measured potential versus Ag/AgCl, $E_{Ag/AgCl}$, was calibrated with respect to the NHE (normal/standard hydrogen electrode), E_{NHE}, according to the Nernst equation [42]. Figure 7(a) shows the data, indicating that Alloy(v) exhibits higher activity for HER compared to Alloy(I, II, III, IV). The rate of HER is directly proportional to the cathodic current density, and Alloy(v) demonstrates the highest current density for hydrogen production, measuring 1.57 $A{\cdot}cm^{-2}$ at a potential of 2.506 V in alkaline medium (1M NaOH). The enhanced activity of Alloy(v) can be attributed to its nanoporous structure, which provides a higher surface area to volume ratio. Additionally, the synergistic combination of Cu, Ni, Fe, Zn, and O in Alloy(v) contributes significantly to its HER activity. The increased content of iron and nickel in the alloy may also enhance the hydrogen evolution rate due to the structural and morphological properties, such as the reticular form of Alloy(v) and the presence of nanogranular structures on the surface, which result in a rough and high surface area. In the case of Alloy(I), it exhibits the lowest HER production rate as it has the lowest ratio of Ni and Fe in its structure and on its surface. Table 3 provides estimated current densities for different electrodes at various potential values and in different mediums. The results from Figure 7 and Table 3 indicate that an increase in Fe% and Ni% leads to higher current density and, consequently, an increased rate of hydrogen production. Furthermore,

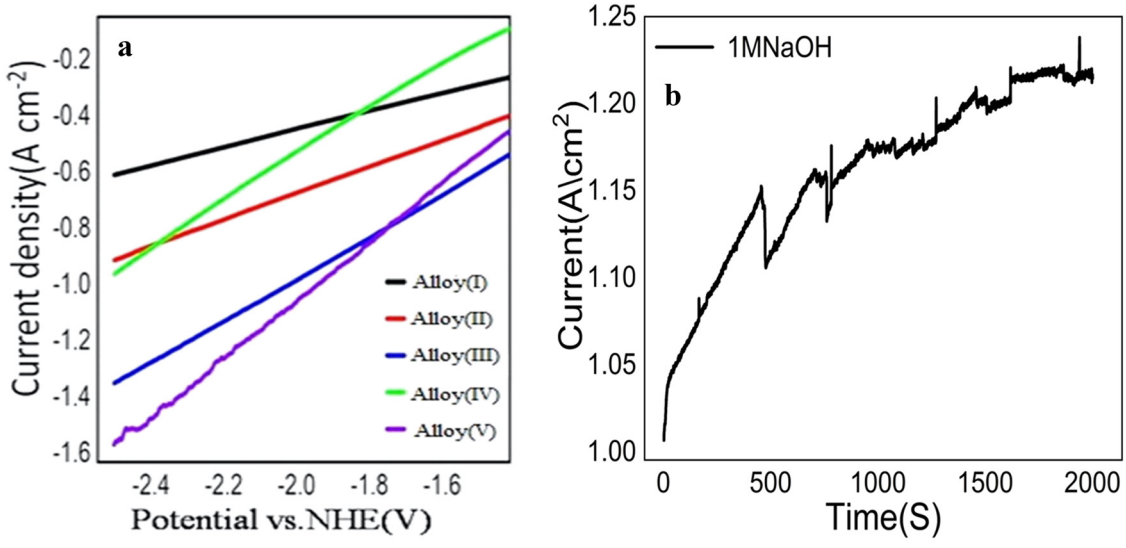

Figure 7: Cathodic polarization for electrodeposited Alloy(I, II, III, IV, V): (a) immersed in stagnant aerated (1 $mol{\cdot}L^{-1}$) NaOH solution at 25°C, NHE (normal/standard hydrogen electrode), (b) relation between time (s) and current density ($mA{\cdot}cm^{-2}$) to study the stability of Alloy(I).

Table 3: Values of H_2 evolution rate of deposited Cu–Fe–Ni–Zn–O alloys dipped in 1 mol L^{-1}NaOH solution at 25°C

Materials	$I_{-2.506V}$ ($A{\cdot}cm^{-2}$)	$I_{-2.3V}$ ($A{\cdot}cm^{-2}$)	$I_{-2.1\ V}$ ($A{\cdot}cm^{-2}$)	$I_{-1.9V}$ ($A{\cdot}cm^{-2}$)	$I_{-1.7V}$ ($A{\cdot}cm^{-2}$)
Medium	NaOH	NaOH	NaOH	NaOH	NaOH
Alloy(I)	−0.61	−0.54	−0.48	−0.41	0.29
Alloy(II)	−0.95	−0.78	−0.61	−0.44	0.34
Alloy(III)	−0.91	−0.82	−0.72	−0.61	0.54
Alloy(IV)	−1.35	−1.2	−1.06	−0.90	0.75
Alloy(V)	−1.57	−1.38	−1.17	−0.96	0.75

applying higher potentials also increases the rate of hydrogen production, as mentioned in the literature [42]. In summary, the findings suggest that Alloy(V) is the most effective for HER, exhibiting higher current densities in alkaline mediums. Figure 7(b) shows the stability and hydrogen production efficiency of the alloy in 1M NaOH over time. The current density gradually increases and stabilizes around 1.2 $A{\cdot}cm^{-2}$, indicating consistent electrochemical performance. This stable current density reflects the alloy's ability to produce hydrogen efficiently through the HER. The absence of significant drops in current density suggests excellent chemical and structural stability of the alloy, even in a highly alkaline environment. Minor fluctuations observed in the graph are likely caused by gas bubble formation during the HER process, which is a typical phenomenon. Despite these fluctuations, the alloy maintains its activity, proving its reliability for long-term use. This high stability and hydrogen production efficiency make the alloy suitable for water splitting applications. Overall, the results highlight the alloy's potential as a durable and effective hydrogen evolution catalyst.

2.6 Electrochemical impedance spectroscopy (EIS) analysis

EIS was employed to validate the electrochemical polarization (ECP) measurements and to investigate the HER kinetics of the electroplated Ni–Fe alloys deposited on brass foil. The EIS measurements were conducted using a galvanostat/potentiostat frequency analyzer coupled with an Autolab 10 potentiostat (Radiometer PGZ100) controlled by software version 4. Figure 8a displays the Nyquist plots for Alloy(I), Alloy(II), Alloy(III), Alloy(IV), and Alloy(V), recorded at potentials relevant to hydrogen evolution. All the investigated alloys exhibited depressed capacitive semicircles, which are characteristic of non-ideal electrochemical interfaces, possibly due to surface roughness or heterogeneities in the alloy coatings. The diameter of the semicircles, which corresponds to the charge transfer resistance (R_{ct}), varied significantly among the different alloy electrodes. A smaller semicircle radius indicates a lower Rct and thus reflects more rapid electron transfer kinetics and superior electrocatalytic activity toward the HER. Among the tested electrodes, Alloy(V) displayed the smallest semicircle diameter, indicating the lowest Rct and therefore the most efficient catalytic behavior for hydrogen evolution, while Alloy(IV) also demonstrated excellent HER activity but was slightly less efficient than Alloy(V). In contrast, Alloy(I) and Alloy(II) exhibited the largest semicircle diameters, implying higher R_{ct} values and slower HER kinetics. Moreover, the Warburg impedance (σ), evident as a linear slope at lower frequencies, revealed mass transport effects associated with hydrogen ion diffusion and gas bubble detachment at the electrode surface; lower σ values suggest enhanced diffusion processes and fewer transport limitations during HER. Repeated EIS

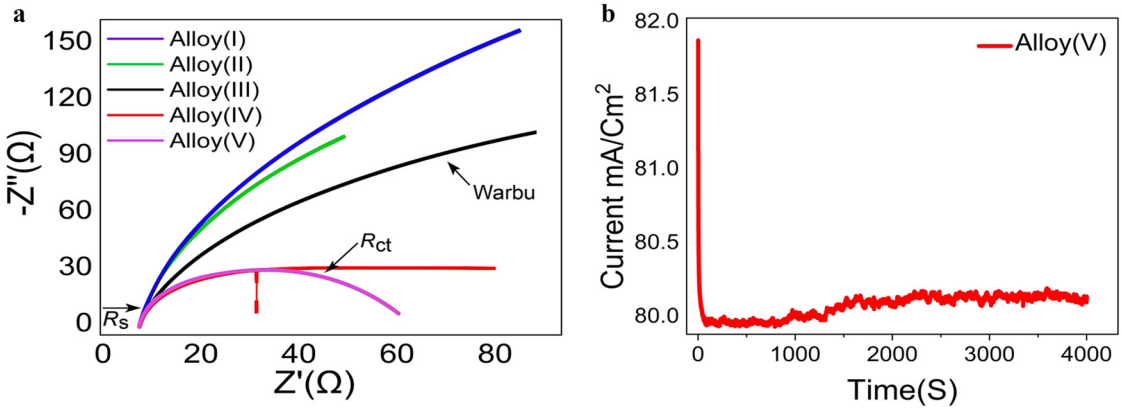

Figure 8: (a) Nyquist plots of electroplated Ni–Fe/Brass foil alloy electrodes (Alloy I, II, III, IV, and V), (b) chronoamperometry stability test for Alloy V.

measurements under prolonged HER conditions revealed that Alloy(v) and Alloy(iv) maintained consistent Nyquist plots with negligible changes in semicircle diameter, confirming their excellent electrochemical stability during hydrogen production. Conversely, Alloy(i) and Alloy(ii) showed increases in semicircle diameters upon repeated cycling, indicating a progressive increase in Rct and suggesting possible surface degradation or loss of active catalytic sites. Thus, Alloy(v) emerged as the most promising electrocatalyst among the studied Ni–Fe alloys, combining the lowest Rct, minimal Warburg impedance, and high operational stability, which are all critical parameters for efficient and durable HER performance. A comparative summary of the measured electrochemical parameters for all alloys is presented in Table 4, highlighting the superior performance of Alloy(v) in terms of both activity and stability.

To further verify the electrochemical stability of Alloy (v) during the HER, a chronoamperometric measurement was conducted by recording the current density as a function of time under a constant applied potential corresponding to HER conditions. Figure 8b shows the current–time curve for Alloy(v), the experiment revealed an initial rapid decrease in current density during the first few seconds, which is commonly attributed to double-layer charging, surface restructuring, and the removal of adsorbed hydrogen bubbles from the electrode surface, all of which contribute to stabilizing the electrode–electrolyte interface. Following this brief initial transient, the current density plateaued and remained nearly constant at approximately 80.0 mA·cm^{-2} over an extended period exceeding 4,000 s, with only minimal fluctuations within ±0.5 mA·cm^{-2}. This steady-state behavior indicates that Alloy(v) maintains its catalytic activity without significant degradation, dissolution, or loss of active sites during prolonged HER operation. Such stability is critical for practical applications, as it ensures sustained hydrogen production efficiency over time. The chronoamperometric results are consistent with the EIS measurements, where Alloy(v) exhibited the lowest charge transfer resistance (R_{ct}) and the smallest Warburg impedance coefficient (σ), confirming both its high intrinsic catalytic activity and its durability under electrochemical stress. Therefore, the combination of low R_{ct}, minimal diffusion limitations, and excellent current retention during long-term HER electrolysis positions Alloy(v) as a highly promising and stable electrocatalyst for hydrogen production applications.

Table 4: EIS parameters and HER performance comparison of Ni–Fe/brass alloys

Alloy	R_s (Ω)	R_{ct} (Ω)	σ (Ω·s$^{-1/2}$)	HER performance
Alloy(v)	2.1	18.2	6.5	Excellent
Alloy(iv)	2.3	24.7	8.3	Very good
Alloy(iii)	2.0	35.9	10.9	Moderate
Alloy(ii)	2.5	45.2	13.7	Poorer
Alloy(i)	2.4	52.8	15.4	Poorest

2.7 Effect of light intensity on the alloy oxide as a photodetector

The effect of light intensity on the photodetection capabilities of the Cu–Fe–Ni–Zn–O burning NPs alloy material was investigated. The tests were conducted using a solar simulator with a power density of 400 mW·cm^{-2} in solution of 0.2M Na_2SO_4. The current density (J_{ph}) values were measured under both dark and light conditions. In the absence of light, the J_{ph} value was found to be 23 mA·cm^{-2} at potential 1 V, as shown in Figure 9, while under light conditions, it significantly increased to 68.45 mA·cm^{-2} at potential 1 V. The high current density under light exposure is primarily due to the photoexcitation of electrons. Upon illumination, the alloy oxide absorbs photons, which excite electrons from the valence band to the conduction band, generating electron–hole pairs (e^-–h^+) [43,44]. This absorption can be attributed to the composition of the alloy oxide, which includes materials like NiO and CuO, known for their ability to harness visible light effectively and for photocatalytic applications. Efficient charge separation and minimized recombination is critical for achieving high photocurrent.

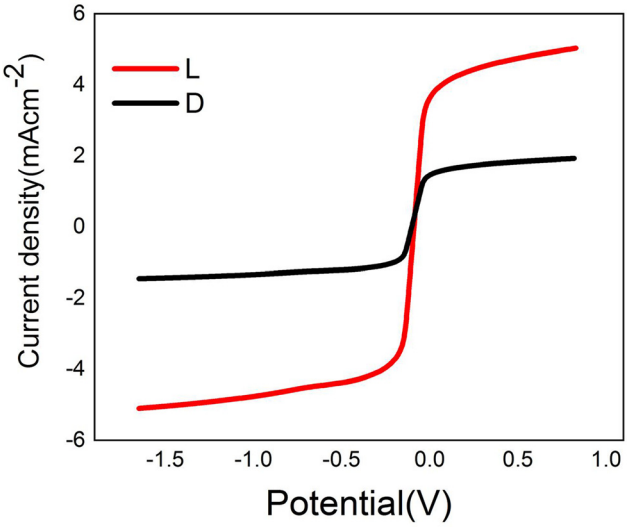

Figure 9: Effect of light intensity on the alloy oxide Cu–Fe–Ni–Zn–O.

The alloy composition with Ni, Cu, and Fe can enhance charge separation and prolong the life of photogenerated carriers. For instance, Fe and Ni sites can trap holes temporarily, thus helping maintain separated e^-–h^+ pairs and reducing recombination [43], [44]. This process can be facilitated further by the layered microstructure observed in alloys with rough and agglomerated surfaces, as these can increase the surface area and provide additional active sites for hydrogen evolution. Alloy oxide composition and structure also play an essential role in charge transport. Nickel and copper oxides, for example, have suitable band gaps for visible light absorption, enhancing the alloy's capability to act as a photoelectrode under solar conditions. This substantial increase in J_{ph} when exposed to light indicates that the Cu–Fe–Ni–Zn–ONPs alloy material is an efficient photodetector.

2.8 Conclusion

Different characterization techniques confirmed the structural and electrochemical properties of the prepared Ni–Fe alloys. Cyclic voltammetry revealed that the optimal Fe/Ni ratio resulted in the thickest alloy layer, while succinic acid significantly enhanced deposition efficiency lowering the reduction potential to –0.77 mV and increasing the peak current to –18 mA. EDX analysis confirmed the high purity of the electrodes. Electrochemical testing using ECP showed that Alloy(v) achieved the highest hydrogen evolution activity, with a current density of 1.57 $A{\cdot}cm^{-2}$ at 2.506 V in 1M NaOH, highlighting its efficiency as an HER electrocatalyst. Additionally, the thermally oxidized alloy showed excellent performance as a photodetector, achieving a photocurrent density of 68.45 $mA{\cdot}cm^{-2}$ under 400 $mW{\cdot}cm^{-2}$ illumination.

Acknowledgments: Dr. Mohammad H. BinSabt gratefully acknowledges the resources of the research sector projects unit (RSPU) general facilities of the Faculty of Science (GFS) (GS01/01, GS01/05, GS02/08), Nanotechnology Research Facility (KUNRF) of the College of Engineering and Petroleum (GE01/07) and Chemistry department at Kuwait University for the use of scanning electron microscopy (SEM).

Funding information: Authors state no funding involved.

Author contributions: Validation and investigation: Islam Kholidy. Methodology, validation, supervision, investigation, writing – review and editing: Muhammad Hussain Bin Sabt, Mohamed Rabia. Methodology, validation, investigation, writing – review and editing: Hanafy Mahmoud Abd El-Salam, Mohamed Shaban.

Conflict of interest: The authors state no conflict of interest.

Data availability statement: All data generated or analyzed during this study are included in this published article.

References

[1] Mahdavi S, Allahkaram SR. Composition, characteristics and tribological behavior of Cr, Co-Cr and Co-Cr/TiO_2 nano-composite coatings electrodeposited from trivalent chromium based baths. J Alloy Compd. 2015;635:150–7. doi: 10.1016/j.jallcom.2015.02.119.

[2] El Awadi GA. Review of effective techniques for surface engineering material modification for a variety of applications. AIMS Mater Sci. 2023;10(4):652–92. doi: 10.3934/matersci.2023037.

[3] Bhat RS, Nagaraj P, Priyadarshini S. Zn–Ni compositionally modulated multilayered alloy coatings for improved corrosion resistance. Surf Eng. 2021;37(12):1430–7. doi: 10.1080/02670844.2020.1812479.

[4] Hong B, Jiang CH, Wang XJ. Texture of electroplated copper film under biaxial stress. Mater Trans. 2006;47(9):2299–301. doi: 10.2320/matertrans.47.2299.

[5] Guan T, Zhang N. Recent advances in electrodeposition of nickel-based nanocomposites enhanced with lubricating nanoparticles. Nanomanuf Metrol. 2024;7(1):25. doi: 10.1007/s41871-024-00245-6.

[6] Chandrasekar MS, Pushpavanam M. Pulse and pulse reverse plating-Conceptual, advantages and applications. Electrochim Acta. 2008;53(8):3313–22. doi: 10.1016/j.electacta.2007.11.054.

[7] Sajjadnejad M, Mozafari A, Omidvar H, Javanbakht M. Preparation and corrosion resistance of pulse electrodeposited Zn and Zn-SiC nanocomposite coatings. Appl Surf Sci. 2014;300:1–7. doi: 10.1016/j.apsusc.2013.12.143.

[8] Torabinejad V, Aliofkhazraei M, Assareh S, Allahyarzadeh MH, Rouhaghdam AS. Electrodeposition of Ni–Fe alloys, composites, and nano coatings – A review. J Alloy Compd. 2017;693:1238–61. doi: 10.1016/j.jallcom.2016.08.329.

[9] Okonkwo BO, Jeong C, Jang C. Advances on Cr and Ni electrodeposition for industrial applications – a review. Coatings. 2022;12(10):1555. doi: 10.3390/coatings12101555.

[10] Giurlani W, Zangari G, Gambinossi F, Passaponti M, Salvietti E, Di Benedetto F, et al. Electroplating for decorative applications: Recent trends in research and development. Coatings. 2018;8(8):260. doi: 10.3390/coatings8080260.

[11] Bagaria SK, Periasamy C. Magnetic properties of electro formed Ni and Ni Fe for micromagnetic MEMS applications. J Supercond Nov Magn. 2015;28:3357–63. doi: 10.1007/s10948-015-3168-5.

[12] Bao M, Wang W. Future of microelectromechanical systems (MEMS). Sens. Actuators, A. 1996;56(1–2):135–41. doi: 10.1016/0924-4247(96)01274-5.

[13] Myung NV, Park DY, Yoo BY, Sumodjo PTA. Development of electroplated magnetic materials for MEMS. J Magn Magn Mater. 2003;265(2):189–98. doi: 10.1016/S0304-8853(03)00264-6.

[14] Bari GADI. Electrodeposition of nickel, modern electroplating: fifth edition. Hoboken, NJ, USA: John Wiley & Sons, Inc.; 2011. p. 79–114. doi: 10.1002/9780470602638.ch3.

[15] Gezerman AO, Corbacioglu BD. Analysis of the characteristics of nickel-plating baths. Int J Chem. 2010;2(2):36–44. doi: 10.5539/ijc.v2n2p124.
[16] Horkans J. Effect of plating parameters on electrodeposited NiFe. J Electrochem Soc. 1981;128(1):45–9. doi: 10.1149/1.2127385.
[17] Myung NV, Nobe K. Electrodeposited iron group thin-film alloys: structure-property relationships. J Electrochem Soc. 2001;148(3):C136. doi: 10.1149/1.1345875.
[18] Wu Y, Chang D, Kim D, Kwon S-C. Influence of boric acid on the electrodepositing process and structures of Ni–W alloy coating. Surf Coat Technol. 2003;173(2–3):259–64. doi: 10.1016/S0257-8972(03)00449-3.
[19] Tsuru Y, Nomura M, Foulkes FR. Effects of boric acid on hydrogen evolution and internal stress in films deposited from a nickel sulfamate bath. J Appl Electrochem. 2002;32(6):629–34. doi: 10.1023/A:1020130205866.
[20] Zech N, Landolt D. The influence of boric acid and sulfate ions on the hydrogen formation in Ni–Fe plating electrolytes. Electrochim Acta. 2000;45(21):3461–71. doi: 10.1016/S0013 4686(00)00415 1.
[21] Gadad S, Harris TM. Oxygen incorporation during the electrodeposition of Ni, Fe, and Ni–Fe alloys. J Electrochem Soc. 1998;145(11):3699–703. doi: 10.1149/1.1838861.
[22] Oriňáková R, Turoňová A, Kladeková D, Gálová M, Smith RM. Recent developments in the electrodeposition of nickel and some nickel-based alloys. J Appl Electrochem. 2006;36(9):957–72. doi: 10.1007/s10800-006-9162-7.
[23] Wei Su C, Jiao He F, Ju H, Bin Zhang Y, Li Wang E. Electrodeposition of Ni, Fe and Ni–Fe alloys on a 316 stainless steel surface in a fluorborate bath. Electrochim Acta. 2009;54(26):6257–63. doi: 10.1016/j.electacta.2009.05.076.
[24] Afshar A, Dolati AG, Ghorbani M. Electrochemical characterization of the Ni-Fe alloy electrodeposition from chloride-citrate-glycolic acid solutions. Mater Chem Phys. 2003;77(2):352–8. doi: 10.1016/S0254-0584(02)00017-2.
[25] Ghorbani M, Dolati AG, Afshar A. Electrodeposition of Ni-Fe alloys in the presence of complexing agents. Russ J Electrochem. 2002;38(11):1173–7. doi: 10.1023/A:1021141524584.
[26] Zhou Y, Wang Z, Cui M, Wu H, Liu Y, Ou Q, et al. NiFe-based electrocatalysts for alkaline oxygen evolution: Challenges, strategies, and advances toward industrial-scale deployment. Adv Funct Mater. 2024;34:2410618. doi: 10.1002/adfm.202410618.
[27] Shetty S. Electrodeposition and characterization of Ni–Mo alloy as an electrocatalyst for alkaline water electrolysis. J Electroanal Chem. 2017;796:1–9. doi: 10.1016/j.jelechem.2017.05.002.
[28] Alnuwaiser MA, Rabia M, Elsayed A. M, Katkar P. K. Paving the way for commercial hydrogen generation from natural and artificial seawater based on photocathode of manganese(II) oxide–manganese(IV) oxide/poly 1H pyrrole nanocomposite seeded on additional poly 1H pyrrole film. Int J Energy Res. 2025;11:9369233. doi: 10.1155/ER/9369233.
[29] Rabia M, Alnuwaiser MA. One pot fabrication of highly porous morphology of ferric oxide ferric oxychloride/poly O chloroaniline nanocomposite seeded on poly 1H pyrrole: Photocathode for green hydrogen generation from natural and artificial seawater. Open Chem. 2025;23(1):20240123,1–11. doi: 10.1515/CHEM 2024 0123.
[30] Alkallas FH, Trabelsi ABG, Rabia M, Boshagh F. Rod-structured manganese oxides/poly-3-methyl benzene amine photocathode without a sacrificial agent for hydrogen production. Int J Energy Res. 2025;2025:9031508. doi: 10.1155/ER/9031508 E.
[31] Aldosari E, Rabia M, Zhang Q, Altilasi HH, Trabelsi ABG, Alkallas FH. Single-step fabrication of Mn(IV) oxide–Mn(II) sulfide/poly-2-mercaptoaniline porous network nanocomposite for pseudo-supercapacitors and charge storage. Open Phys. 2025;23(1):1–11. doi: 10.1515/phys-2025-0132.
[32] Menaka SM, Umadevi G, Maheswari AU. Spray deposition and characterization of p-type Li doped NiO Thin films. Int J Thin Films Sci Tec. 2019;8(2):61–6. doi: 10.18576/ijtfst/080205.
[33] Biesinger MC, Lau LWM, Gerson AR, Smart RSC. The role of the auger parameter in XPS studies of nickel metal, halides and oxides. Phys Chem Chem Phys. 2012;14(7):2434–42. doi: 10.1039/c2cp22419d.
[34] Dubey P, Ravrupesh AN, Devan S, Okram GS, Kuod YK. The effect of stoichiometry on the structural, thermal and electronic properties of thermally decomposed nickel oxide. RSC Adv. 2018;8:5882. doi: 10.1039/c8ra00157.
[35] Ratcliff E L, Meyer J, Steirer KX, Garcia A, Berry JJ, Ginley DS, et al. Evidence for near-surface NiOOH species in solution-processed NiOx selective interlayer materials: impact on energetics and the performance of polymer bulk heterojunction photovoltaics. Chem Mater. 2011;23(22):4988–5000. doi: 10.1021/cm202296p.
[36] Biesinger M C, Payne BP, Lau LWM, Gerson A, Smart RSC. X ray photoelectron spectroscopic chemical state quantification of mixed nickel metal, oxide and hydroxide systems. Surf Interface Anal. 2009;41(4):324–32. doi: 10.1002/sia.3026.
[37] Valentine JG, Street RA, Bradley DDC, Silva SRP, Amaratunga GAJ. X ray photoelectron spectroscopic investigation of plasma enhanced chemical vapor deposition and electrocatalytic characterization of pure NiO_x and $NiO_x(OH)_y$. J Phys Chem C. 2017;121(12):6521–30. doi: 10.1021/acs.jpcc.6b12652.
[38] Huang L, Peng F, Ohuchi FS. In situ' XPS study of band structures at Cu_2O/TiO_2 heterojunctions interface. Surf Sci. 2009;603(17):2825–34. doi: 10.1016/j.susc.2009.07.030.
[39] Ai Z, Zhang L, Lee S, Ho W. Interfacial hydrothermal synthesis of $Cu@Cu_2O$ core - Shell microspheres with enhanced visible-light-driven photocatalytic activity. J Phys Chem C. 2009;113(49):20896–902. doi: 10.1021/jp9083647.
[40] Liu Y, Zhang H, Fu W, Yang Z, Li Z. Characterization of temperature sensitivity of V-modified CuFe2O4 ceramics for NTC thermistors. J Mater Sci: Mater Electron. 2018;29(21):18797–806. doi: 10.1007/s10854-018-0005-1.
[41] Kholidy I, BinSabt MH, Abd El-Salam HM, Shaban M, Rabia M. Improved electrochemical synthesis of Cu–Fe/brass foil alloy followed by combustion for high-efficiency photoelectrodes and hydrogen production in alkaline solutions. Green Process Synth. 2025;14(1):20240137. doi: 10.1515/gps-2024-0137.
[42] Shaban M, Kholidy I, Ahmed GM, Negem M, Abd El-Salam HM. Cyclic voltammetry growth and characterization of Sn–Ag alloys of different nanomorphologies and compositions for efficient hydrogen evolution in alkaline solutions. RSC Adv. 2019;9:22389. doi: 10.1039/c9ra03503f.
[43] Elsayed AM, Rabia M, Shaban M, Aly AH, Ahmed AM. Preparation of hexagonal nanoporous Al_2O_3/TiO_2/TiN as a novel photodetector with high efficiency. Sci Rep. 2021;11(1):1–12. doi: 10.1038/s41598-021-96200-2.
[44] Abdelazeez AAA, Hadia NMA, Alzaid M, Shaban M, Mourad AHI, Fernández S, et al. Development of CuO nanoporous material as a highly efficient optoelectronic device. Appl Phys A Mater Sci Process. 2022;128(4):321. doi: 10.1007/s00339-022-05447-7.